21, rue d'Artois, F-75008 PARIS
http : //www.cigre.org

CIGRE US National Committee
2013 Grid of the Future Symposium

Control of Brushless Doubly-Fed Reluctance Wind Generators

S. ADEMI, M. JOVANOVIĆ, J. K. OBICHERE
Faculty of Engineering and Environment
Northumbria University, Newcastle upon Tyne, United Kingdom

SUMMARY

The paper is concerned with field-oriented control (FOC) and vector control (VC) of a promising brushless doubly-fed reluctance generator (BDFRG) technology for adjustable speed wind turbines with maximum power point tracking. The BDFRG has been receiving increasing attention because of the low capital and operation & maintenance costs afforded by using partially-rated power electronics and the high reliability of brushless design, while offering performance competitive to its well-known slip-ring counterpart, a doubly-fed induction generator (DFIG). The preliminary studies have evaluated the performance of the two robust, parameter independent control algorithms on a custom-made BDFRG under the maximum torque per inverter ampere (MTPIA) conditions to allow the improved efficiency of the generator-converter set and therefore the entire wind energy conversion system. Although the controllers have been tested and their high potential demonstrated on a small-scale level under the most challenging conditions from a control point of view, they are versatile in nature and generally applicable to large generators (e.g. 2 MW BDFRG designs have already been reported in the literature) as well where they should perform even better (especially FOC) with the winding resistive effects and dynamic requirements (e.g. large lumped inertia constants) being much less pronounced.

KEYWORDS

Wind Power, Brushless, Doubly-Fed Reluctance Machines, Control.

E-mail: milutin.jovanovic@northumbria.ac.uk

1. Introduction

The brushless doubly-fed reluctance generators (BDFRGs) have been considered as a viable alternative to conventional slip-ring doubly-fed induction generators (DFIGs) for grid-connected wind turbines where only a limited variable speed capability is required (e.g. typically, a 2:1 range or so around the synchronous speed) [1–3]. The BDFG would allow to retain the same DFIG cost benefits of using a smaller inverter (e.g. around 25% of the machine rating), but with higher reliability and maintenance-free operation by the absence of brush gear.

Unlike the DFIG, the BDFRG has two standard stator windings of different applied frequencies and pole numbers, and a cage-less reluctance rotor [4] with half the total number of stator poles to provide the rotor position dependent magnetic coupling between the windings, a pre-requisite for the torque production [5, 6]. The primary (power) winding is grid-connected, and the secondary (control) winding is supplied from a bi-directional (‘back-to-back’) dual-bridge power converter (Fig. 1). The BDFRG offers the prospect for higher efficiency [7] with simpler modelling and control than its ‘nested’ cage rotor form, the brushless doubly-fed induction generator (BDFIG) [8–10]. Control of the primary reactive power and electromagnetic torque is inherently decoupled in both the BDFRG and DFIG [11], but not in the BDFIG [8, 10]. Another important BDFR(I)G merit is the seemingly superior low-voltage-fault-ride-through capability to the DFIG, which may be accomplished safely without a crowbar circuitry owing to the larger leakage inductances and thus the lower fault current levels [12, 13].

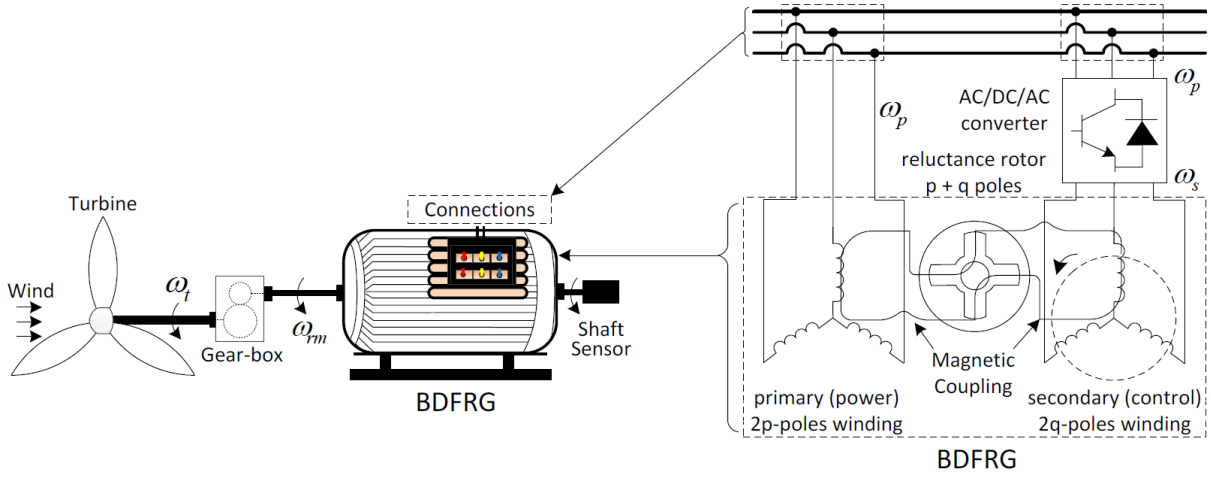

Fig. 1: A structural diagram of the BDFRG based wind energy conversion system

Various control methods have been developed for the BDFRG including scalar control [1, 14], field-oriented control (FOC) [1, 11, 14], direct torque control [14, 15], torque and reactive power control [16, 17], and direct power control [18]. Although their comparative qualitative analysis has been partly made in [14], no similar quantitative study has been reported specifically on FOC vs VC, and there has been no or very little work published on true vector control (VC) of the machine side converter. In the BDFRG case, the ‘FOC/VC’ are commonly being referred to as the primary winding flux/voltage oriented control by analogy to the stator flux/voltage oriented control of the DFIG.

The fact is that with a proper selection of the reference frames, the two control techniques indeed become very similar in nature and dynamic response, especially with larger machines of lower resistances [2, 3]. Nevertheless, they have differences and performance trade-offs to be pointed out in this paper using the maximum torque (power) per inverter ampere (MTPIA) strategy [1, 5] as a ground for their comparison on a custom built BDFRG prototype. The motivation for looking at this control objective is the efficiency gain that can be achieved in wind energy conversion systems (WECS) by reducing both the secondary winding copper and the inverter switching losses [1, 5] of the generator-converter combination itself. Extensive realistic simulation results taking into account the usual practical effects (e.g. transducers' DC offset, noise in measurements, and a four-quadrant power converter model with space-vector PWM) are presented to support the discussions.

2. BDFRG Fundamentals

The basic angular velocity relationship for the electro-mechanical energy conversion in the machine with p_r rotor poles and $\omega_{p,s} = 2\pi f_{p,s}$ applied frequencies (rad/s) to the respective $2p$-pole and $2q$-pole windings (Fig. 1) is [6]:

$$\omega_{rm} = \frac{\omega_p + \omega_s}{p_r} = \frac{(1-s)\cdot\omega_p}{p+q} = (1-s)\cdot\omega_{syn} \Leftrightarrow n_{rm} = 60\cdot\frac{f_p + f_s}{p_r} \quad (1)$$

where the primary and secondary winding are denoted by the subscripts 'p' and 's' respectively, the 'generalised' slip is $s = -\omega_s/\omega_p$ and $\omega_{syn} = \omega_p/p_r$ is the synchronous speed (for $\omega_s = 0$ i.e. a DC secondary) as with a $2p_r$ – pole wound-rotor synchronous turbo-machine. Note that $\omega_s > 0$ for 'super-synchronous' operation, and $\omega_s < 0$ at 'sub-synchronous' speeds (i.e. an opposite phase sequence of the secondary to the primary winding). The two speed modes of the BDFRG are equivalent to a $2p_r$ -pole induction generator (i.e. $s < 0$) despite the quite distinct operating principles [6].

The machine instantaneous torque, and the rotor movement (i.e. the acceleration torque) taking into account the friction terms, can be expressed as follows [6]:

$$T_e = \frac{3p_r L_{ps}}{2L_p}\left(\lambda_{pd} i_{sq} + \lambda_{pq} i_{sd}\right) = \frac{3p_r}{2}\left(\lambda_{ps_d} i_{sq} - \lambda_{ps_q} i_{sd}\right) = \frac{3p_r}{2}\left(\lambda_{pd} i_{pq} - \lambda_{pq} i_{pd}\right) \quad (2)$$

$$T_a = J\frac{d\omega_{rm}}{dt} = T_e - T_L(\omega_{rm}) - F\omega_{rm} \quad (3)$$

where λ_{ps} is the primary flux linking the secondary winding (i.e. the mutual flux linkage). The definitions of the 3-phase self ($L_{p,s}$) and mutual (L_{ps}) inductances can be found in [6]. While the primary flux and current space vectors in (2) are in ω_p rotating frame, the corresponding secondary counterparts, including the λ_{ps} dq components, are in $p_r\omega_{rm} - \omega_p = \omega_s$ frame according to (1) and the BDFRM theory in [6]. This selection maps the variables into their natural reference frames where they appear as DC quantities which are easier to control. Given that λ_p and λ_{ps} in (2) are approximately constant by the primary winding grid connection, torque control can be achieved through the secondary dq currents in the ω_s frame.

Using (1), one can derive the mechanical power equation showing individual contributions of each winding:

$$P_m = T_e\cdot\omega_{rm} = \frac{T_e\cdot\omega_p}{p_r} + \frac{T_e\cdot\omega_s}{p_r} = P_p\cdot\left(1 + \frac{\omega_s}{\omega_p}\right) = P_p\cdot(1-s) \quad (4)$$

The machine operating mode is determined by the power flow in the primary winding i.e. to the grid for the BDFRG when $T_e < 0$ in (4). The secondary winding can either take or deliver real power (P_s) subject to its phase sequence i.e. the ω_s sign: the BDFRG would absorb (produce) $P_s > 0$ at sub (super)-synchronous speeds. Note that (1) and (4) are the same form expressions used for classical induction machines with P_p and ω_s playing the role of rotor power and slip frequency, respectively.

3. Controller Design

A structural block-diagram of the primary voltage/flux angle and frequency estimation technique for FOC/VC algorithms is shown in Fig. 2. The entire BDFRG system configuration with a generic controller design is presented Fig. 3. A conventional vector controller with space-vector PWM of the active rectifier (e.g. the line-side IGBT converter) has been implemented for control of the DC link voltage and unity line power factor [19]. The primary real (P) and reactive (Q) power have been calculated using the stationary frame voltage ($v_{\alpha\beta}$) and current ($i_{\alpha\beta}$) components (Fig. 3) despite the fact that the control has actually been done in the rotating secondary d_s-q_s frame (Fig. 2). Considering that the power calculations are reference frame invariant, this is the least computationally intensive approach for the controller as unnecessary frame conversions and the use of time-consuming trigonometric functions, can be avoided with immediately obvious implications on the higher control rates and superior performance achievable in practice.

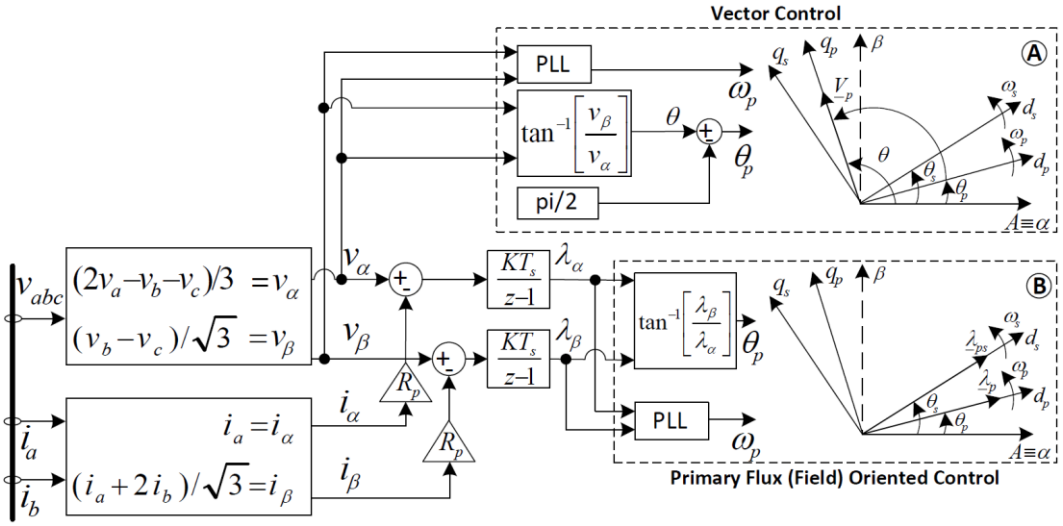

Fig. 2: Identification of primary voltage and flux vectors in a stationary α-β frame

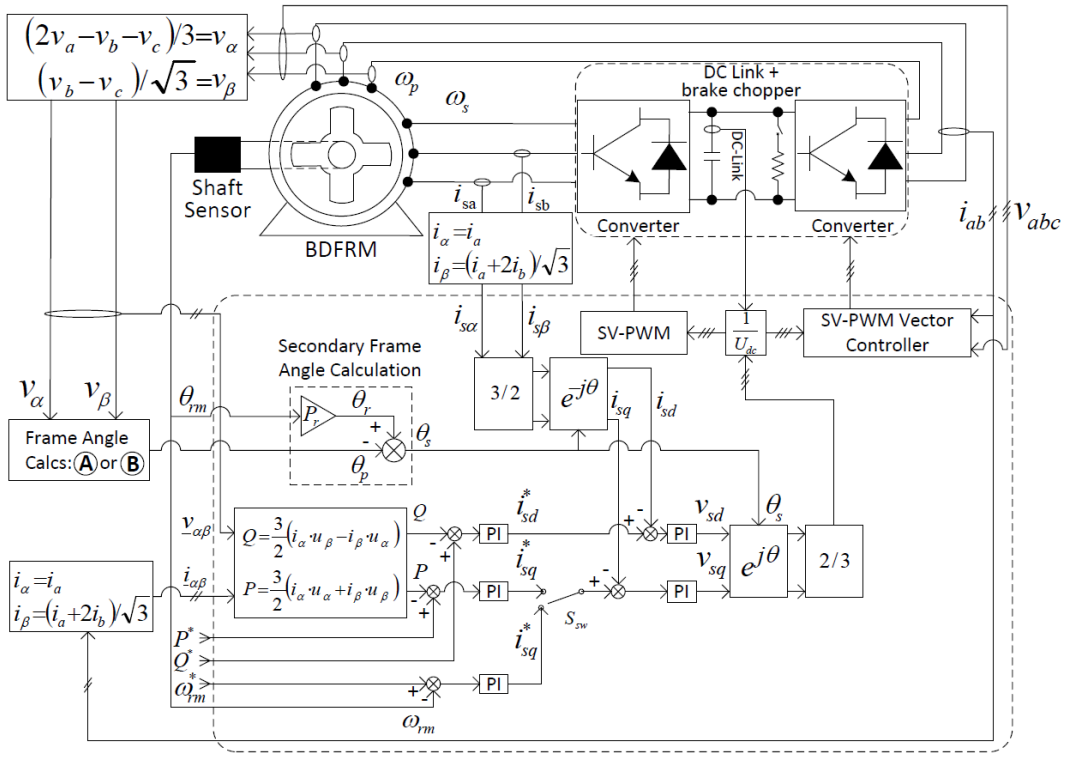

Fig. 3: Structure of a BDFRG(M) drive setup with power electronics control

4. Control Principles

4.1. Vector Control (VC)

Using the BDFRG space-vector model [6], the following steady-state relationships for the primary mechanical power and reactive power can be established:

$$P_{p_{vc}} = \frac{3\omega_p}{2}\left(\lambda_{ps_d} i_{sq} - \lambda_{ps_q} i_{sd}\right) = P_{p_{foc}} - \frac{3}{2}\omega_p \lambda_{ps_q} i_{sd} \quad (5)$$

$$Q_{p_{vc}} = \frac{3\omega_p}{2}\left(\frac{\lambda_p^2}{L_p} - \lambda_{ps_d} i_{sd} - \lambda_{ps_q} i_{sq}\right) = Q_{p_{foc}} - \frac{3}{2}\omega_p \lambda_{ps_q} i_{sq} \quad (6)$$

Note that (5) could have also been derived using (2) and (4).

VC of P_p and Q_p is coupled as both the i_{sd} and i_{sq} secondary currents appear in (5) and (6). The level of coupling can be reduced by aligning the q_p-axis of the reference frame to the primary voltage vector as in Fig. 2. In this case, the primary flux vector ($\underline{\lambda}_p$) would be phase shifted ahead of the corresponding d_p-axis depending on the winding resistance values. This angular displacement is small with larger machines having lower resistances. Therefore, for the frame alignment choice in Fig. 2, VC should be similar to FOC as $\lambda_{ps_d} >> \lambda_{ps_q}$ i.e. $\lambda_{ps_d} \approx \lambda_{ps}$ so that (5) and (6) become:

$$P_{p_{vc}} \approx P_{p_{foc}} = \frac{3}{2}\omega_p \lambda_{ps} i_{sq} = \frac{3}{2}\frac{L_{ps}}{L_p}\omega_p \lambda_p i_{sq} \tag{7}$$

$$Q_{p_{vc}} \approx Q_{p_{foc}} = \frac{3\omega_p}{2}\frac{\lambda_p^2}{L_p} - \frac{3}{2}\omega_p \lambda_{ps} i_{sd} = \frac{3}{2}\frac{\omega_p \lambda_p}{L_p}\left(\lambda_p - L_{ps} i_{sd}\right) = \frac{3}{2}\omega_p \lambda_p i_{pd} \tag{8}$$

With the λ_p and λ_{ps} magnitudes being fixed by the primary winding grid connection at line frequency (ω_p), the P_p vs i_{sq} and Q_p vs i_{sd} relationships above are nearly linear which justifies the use of PI power controllers in Fig. 3. Feed-forward compensation for coupling terms in (5) and (6) may achieve decoupled control similar to FOC but at the expense of having to know the machine inductances.

4.2. Field-Oriented Control (FOC)

The primary flux oriented (e.g. with the reference frame d_p-axis aligned to $\underline{\lambda}_p$ as in Fig. 2) form of (2) simplifies to [6, 11, 14]:

$$T_e = \frac{3p_r L_{ps}}{2L_p}\lambda_p i_{sq} = \frac{3p_r}{2}\lambda_{ps} i_{sq} = \frac{3p_r}{2}\lambda_p i_{pq} \tag{9}$$

The corresponding real and reactive power can now be expressed by (7) and (8).

The most important advantage of FOC over VC of the BDFRG (and the DFIG) is the inherently decoupled control of P_p (or T_e) and Q_p through i_{sq} and i_{sd} variations, respectively, which is immediately obvious from (7) - (9). In favour of VC, it is fair to say that these appealing FOC properties come at the cost of the $\underline{\lambda}_p$ angle estimation (θ_p in B block of Fig. 2) and difficulties with suppressing the detrimental DC offset effects on the voltage integration accuracy. In addition, the primary winding resistance may need to be known in low to medium power applications. As entirely parameter independent, the VC approach clearly does not suffer from any of these FOC limitations.

5. BDFRG Operating Conditions

The viability and performance comparisons of the FOC/VC schemes in Fig. 3 has been demonstrated on a 6/2-pole proof-of-concept machine rated at: 415 V, 2.5 A (for both Y connected windings), 1.5 kW, 750 rev/min, 50 Hz. The remaining BDFRG parameters, obtained by off-line testing as described in [7], are as follows: R_p = 11.1 Ω, R_s = 13.5 Ω, L_p = 0.41 H, L_s = 0.57 H and L_{ps} = 0.34 H. A realistic Simulink® model has been built by: (i) Using the power electronic models from the SimPowerSystems® library; (ii) Superimposing the high-frequency uncorrelated white noise and unknown slowly varying DC offset to the ideal signals to account for practical effects of the measurement noise and current/voltage transducers errors; (iii) Assuming that both the rotor position and speed information has been provided by a shaft sensor (e.g. an incremental encoder in our case).

A geared wind turbine has been usually operated in a variable speed range of 2:1 or so. For the 6/2-pole example BDFRG, this is $[n_{min} = 500, n_{max} = 1000\ ]$ rev/min i.e. 250 rev/min around a synchronous speed of $n_{syn} = 750$ rev/min for the $f_p = 50$ Hz supply, the boundary secondary frequencies of $f_s = \pm f_p/3$ and the respective 'slip' limits of $s = -f_s/f_p = \mp 1/3$ according to (1). It can be easily shown using (4) that $P_s \approx 0.25 \cdot P_m$ meaning that the inverter would need to handle at most 25% of the mechanical power (plus total losses on the secondary side).

The turbine output torque on the generator side for the maximum wind energy extraction in the base speed region (i.e. between the minimum 'cut-in', u_{min}, and the rated wind speed, u_r), can be represented as [1, 3]:

$$T_{opt} = \frac{A \cdot \rho \cdot C_p(\lambda_{opt}, \gamma) \cdot R^3}{2 \cdot g^3 \cdot \lambda_{opt}^3} \cdot \omega_{rm}^2 = K_{opt} \cdot \omega_{rm}^2 \tag{10}$$

where ρ is the air density, $C_p\ (\lambda,\gamma)$ is the power (performance) coefficient (i.e. the maximum turbine efficiency as $\lambda = \lambda_{opt}$ in this case), $\lambda_{opt} = R\omega_t^*/u$ is the optimum tip speed ratio for a given wind speed

u, ω_t^* is the turbine rotor angular velocity for MPPT, γ is the pitch angle (normally fixed to zero to maximise C_p), R is the blade length (i.e. the radius of the circular swept area, $A = \pi R^2$), and $g = \omega_{rm}^*/\omega_t^*$ is the gear ratio where ω_{rm}^* is the desired (reference) velocity to be achieved (Fig. 3). The main task of the gear-box is to provide mapping of the actual wind and generator operating speed ranges i.e. [u_{min}, u_r] and [n_{min},n_{max}] through an appropriate g value. In practice, the latter is normally chosen to allow matching of the respective mid-range speeds, (u_{min} + u_r)/2 and (n_{min} + n_{max})/2 (= n_{syn} for the BDFRG or DFIG). At gusty wind speeds beyond ur and up to the 'cutout' limit, C_p has to be sacrificed to avoid generator overloading. However, issues related to constant power control of the turbine are out of scope of this paper.

The simulated BDFRG has been assumed to have a shaft torque-speed profile of the same form as (10) to be used in (3) for computer studies:

$$T_L = -T_r \cdot \left(\frac{\omega_{rm}}{\omega_{max}}\right)^2 = -\frac{P_r}{\omega_{syn}} \cdot \left(\frac{n_{rm}}{n_{max}}\right)^2 \approx -19.1 \cdot \left(\frac{n_{rm}}{1000}\right)^2 \text{Nm} \qquad (11)$$

6. Preliminary Results

The simulation results below have been produced by running the FOC and VC algorithms in Fig. 3 in speed mode at 0.1 ms sampling time i.e. the 10 kHz switching rate of the IGBT converter. The DC link voltage has been maintained at 600 V by the PWM rectifier (i.e. the line-side bridge) supplied at 415 V, 50 Hz. The MTPIA strategy [1, 5] has been implemented in Fig. 3 by setting the Q_p^* value for $i_{sd} = 0$ and $\lambda_p \approx u_p/\omega_p$ in (8).

Fig. 4 demonstrates an excellent speed tracking with no overshoot of the test BDFRG operating at synchronous (750 rev/min), super-synchronous (900 rev/min) and sub-synchronous (600 rev/min) speeds in the secondary frequency range of $f_s = \pm 10$ Hz.The reference speed trajectory has been set as a ramp for dynamically not demanding target applications such as wind turbines. Note that the speed response is virtually identical for either the FOC or VC.

The monitored primary electrical power (P) and estimated electro-magnetic torque (T_e) in Fig. 4 reflect the BDFRG input conditions represented by (11) in the control region following the machine start-up. Except for a difference in losses, and considering that $\omega_p \approx$ const by the primary winding grid-connection, P and T_e are directly related as follows from (4) and (5) which explains a close resemblance in shape of the two waveforms. The T_e deviations from the desired load profile during the speed transients refer to the acceleration or deceleration torque term in (3) depending on whether the machine is to speed-up ($T_a > 0$) or slow-down ($T_a < 0$). One can also hardly see any disparity between the FOC and VC results for either P or T_e given (5) and (7).

The primary reactive power (Q) has been directly controlled at 1340 VAr (Fig. 4) to minimise the i_s magnitude for a given shaft torque and therefore achieve the desired MTPIA performance. Note that the Q behaviour with the decoupled FOC is largely unaffected by the P variations. However, the VC waveform is rather distorted and looks like a scaled mirror image of the P counterpart due to the cross-coupling (i_{sq}) term in (6).

The secondary current components ($i_{sd,q}$) and their primary winding equivalents ($i_{pd,q}$) under the MTPIA conditions are presented in Fig. 5. The transient over-currents are clearly avoided by the PI regulators not having to be saturated to allow accurate tracking of the desired trajectories for the moderately varying command speeds in a trapezoidal manner (Fig. 4). The $i_{sd} \approx 0$ as expected for the minimum secondary current loading, while the i_{pd} is required to establish the machine flux and to satisfy the specific Q_p demand according to (8). A close analogy between the active q currents and the complementary real power (torque), as well as the magnetising d currents and Q, is immediately visible from the relevant waveforms in Figs. 4 and 5. The cross-coupling effects of the isq clearly manifest themselves as speed dependent disturbance in the respective non-controllable i_{pd} profiles (Fig. 5) in the VC case similarly to the P and Q situation in Fig. 4. The corresponding FOC i_{pd} (and Q) levels are however constant in average sense throughout the entire speed range.

Fig. 6 shows the step-wise PWM sector change of the modulated secondary voltage vector ($\underline{v}_s$) during a speed reduction from 900 rev/min to 600 rev/min. In the super-synchronous mode, $\underline{v}_s$ rotates anti-clockwise as indicated by the ascending sector numbers for the same phase sequence of the windings when $\omega_s > 0$ in (1). At sub-synchronous speeds, on the other hand, $\underline{v}_s$ rotates clockwise with

the sector numbers descending which comes from the opposite phase sequence of the secondary to the primary winding since $\omega_s < 0$ in (1). Notice that $\underline{v}_s$ becomes stationary at synchronous speed (750 rev/min) as the secondary currents are then DC i.e. $\omega_s = 0$ in (1).

7. Conclusions

The main contribution of the paper is the comparative development and performance analysis of field (primary flux) oriented control (FOC) and vector (primary voltage oriented) control (VC) algorithms for optimum operation of the BDFRG, a viable competitor to DFIG. Such a control framework can serve as a basis for further research on this emerging brush-less machine topology for slip-power recovery applications including wind turbines or pump drives where the cost advantages of partially-rated power electronics can be fully exploited. The realistic simulation studies taking into account the usual practical effects as transducer DC offsets and noise in measurements have clearly illustrated the high potential and effectiveness of the considered control methods using the maximum torque per inverter ampere strategy which offers the machine efficiency improvement.

BIBLIOGRAPHY

[1] M. G. Jovanovic, R. E. Betz, J. Yu, The use of doubly fed reluctance machines for large pumps and wind turbines, IEEE Transactions on Industry Applications 38 (2002) 1508– 1516.

[2] D.G.Dorrell, M.Jovanovic, On the possibilities of using a brushless doubly-fed reluctance generator in a 2 MW wind turbine, IEEE IAS Annual Meeting (2008) 1–8.

[3] F. Valenciaga, P. F. Puleston, Variable structure control of a wind energy conversion system based on a brushless doubly fed reluctance generator, IEEE Transactions on Energy Conversion 22 (2) (2007) 499–506.

[4] A. Knight, R. Betz, D. Dorrell, Design and analysis of brushless doubly fed reluctance machines, IEEE Transactions on Industry Applications 49 (1) (2013) 50–58.

[5] R. E. Betz, M. G. Jovanovic, Theoretical analysis of control properties for the brushless doubly fed reluctance machine, IEEE Transactions on Energy Conversion 17 (2002) 332–339.

[6] R. E. Betz, M. G. Jovanovic, Introduction to the space vector modelling of the brushless doubly-fed reluctance machine, Electric Power Components and Systems 31 (8) (2003) 729–755.

[7] F.Wang, F.Zhang, L.Xu, Parameter and performance comparison of doubly-fed brushless machine with cage and reluctance rotors, IEEE Transactions on Industry Applications 38 (5) (2002) 1237-1243.

[8] J. Poza, E. Oyarbide, I. Sarasola, M. Rodriguez, Vector control design and experimental evaluation for the brushless doubly fed machine, IET EPA 3 (4) (2009) 247–256.

[9] K. Protsenko, D. Xu, Modeling and control of brushless doubly-fed induction generators in wind energy applications, IEEE Transactions on Power Electronics 23 (3) (2008) 1191 –1197.

[10] S. Shao, E. Abdi, F. Barati, R. McMahon, Stator-flux-oriented vector control for brushless doubly fed induction generator, IEEE Trans. on Ind. Electronics 56 (10) (2009) 4220 –4228.

[11] L. Xu, L. Zhen, E. Kim, Field-orientation control of a doubly excited brushless reluctance machine, IEEE Transactions on Industry Applications 34 (1) (1998) 148–155.

[12] T. Long, S. Shao, P. Malliband, E. Abdi, R. McMahon, Crowbarless fault ride-through of the brushless doubly fed induction generator in a wind turbine under symmetrical voltage dips, IEEE Transactions on Industrial Electronics 60 (7) (2013) 2833–2841.

[13] S. Shao, T. Long, E. Abdi, R. A. McMahon, Dynamic control of the brushless doubly fed induction generator under unbalanced operation, IEEE Transactions on Industrial Electronics 60 (6) (2013) 2465–2476.

[14] M. Jovanovic, Sensored and sensorless speed control methods for brushless doubly fed reluctance motors, IET Electric Power Applications 3 (6) (2009) 503–513.

[15] M. G. Jovanovic, J. Yu, E. Levi, Encoderless direct torque controller for limited speed range applications of brushless doubly fed reluctance motors, IEEE Transactions on Industry Applications 42 (3) (2006) 712–722.

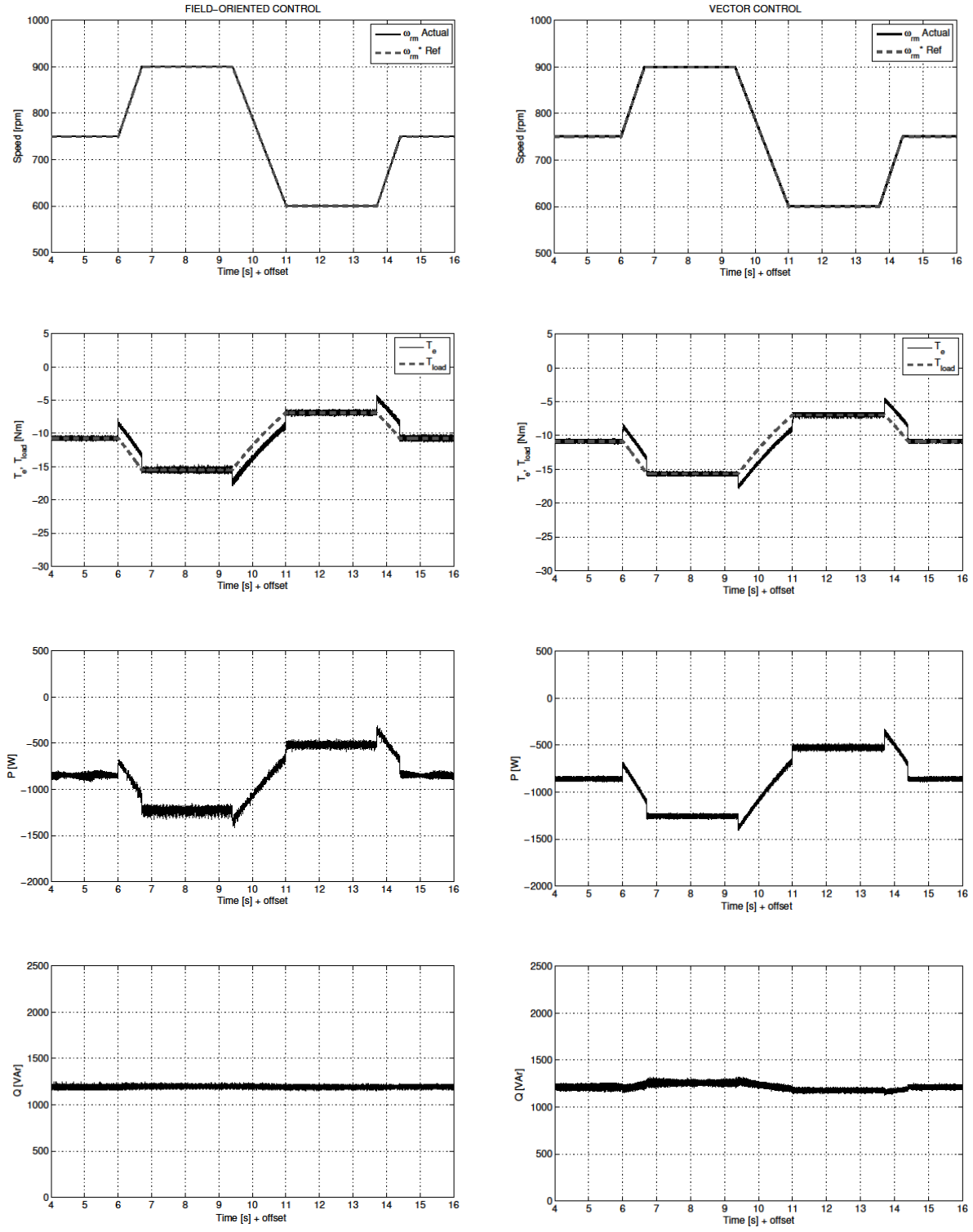

Fig. 4: BDFRG speed, torque, and primary real/reactive power response to reference speed-torque variations in a limited range around synchronous speed

[16] H. Chaal, M. Jovanovic, Practical implementation of sensorless torque and reactive power control of doubly fed machines, IEEE Trans. on Ind. Electronics 59 (6) (2012) 2645–2653.

[17] H. Chaal, M. Jovanovic, Toward a generic torque and reactive power controller for doubly fed machines, IEEE Transactions on Power Electronics 27 (1) (2012) 113–121.

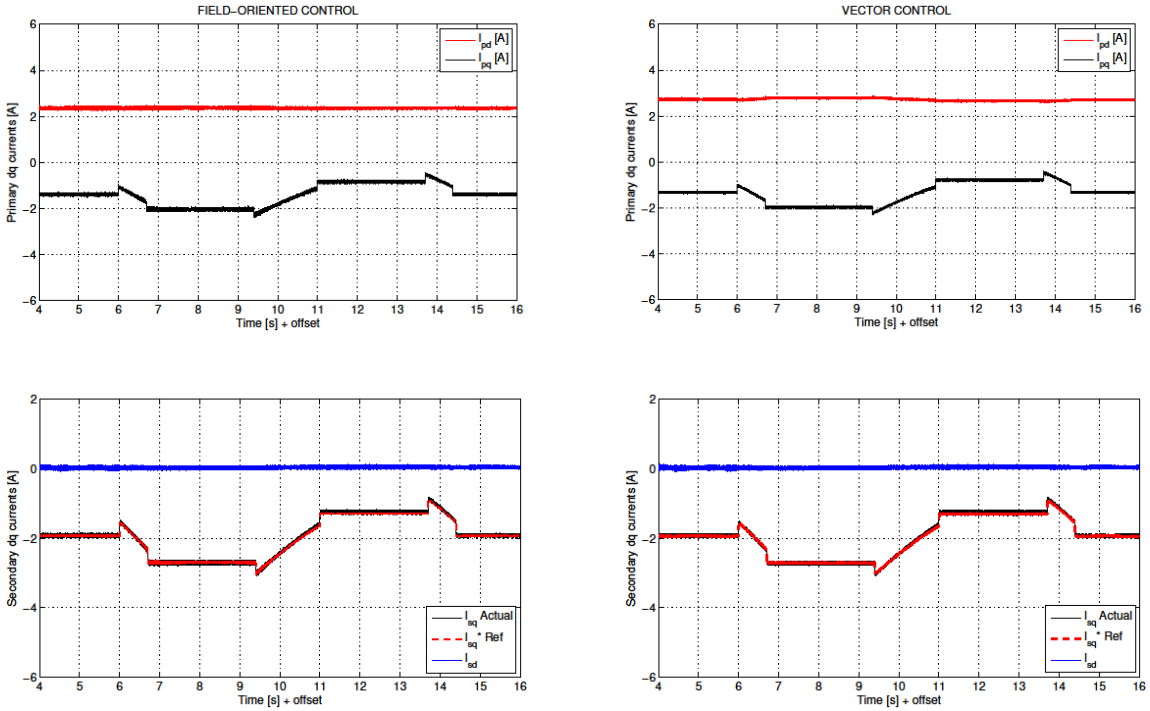

Fig. 5: BDFRG MTPIA *dq* currents in the respective frames complementing the results in Fig. 4

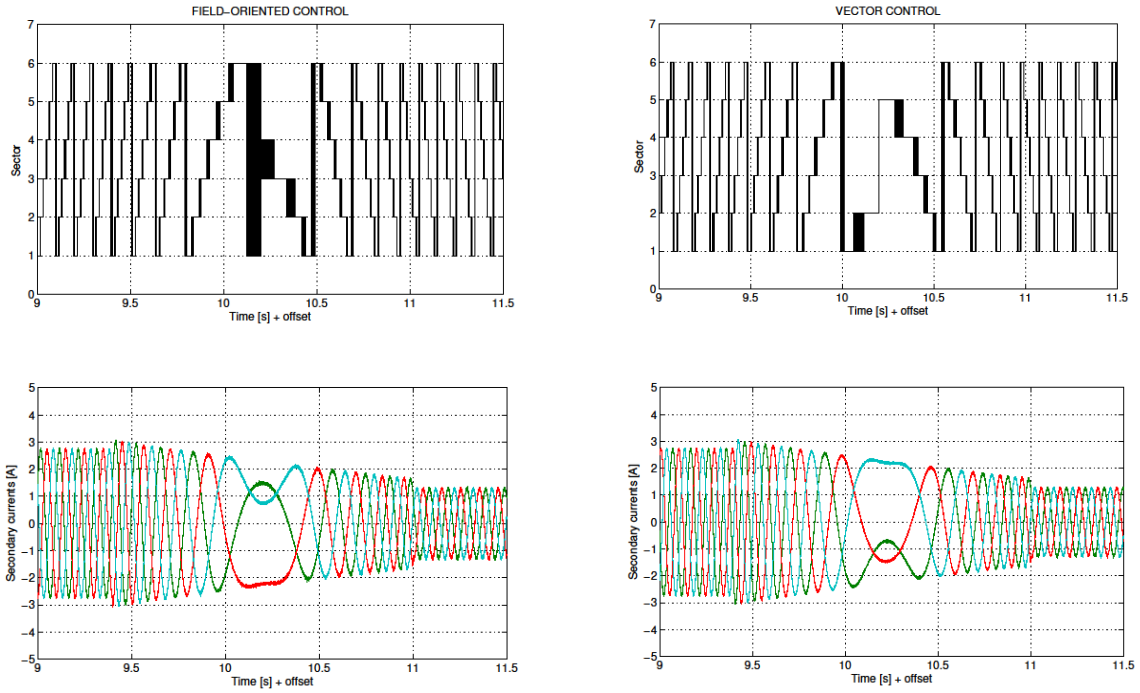

Fig. 6: BDFRG inferred secondary voltage positions and secondary current waveforms showing a phase sequence reversal during the transition from super- to sub-synchronous speed mode

[18] H. Chaal, M. Jovanovic, Power control of brushless doubly-fed reluctance drive and generator systems, Renewable Energy 37 (1) (2012) 419–425.

[19] R.Pena, J.C.Clare, G.M.Asher, Doubly fed induction generator using back-to-back PWM converters and its application to variable-speed wind-energy generation, IEE Proc. - Electr. Power Appl. 143 (3) (1996) 231–241.